Journal of Materials Chemistry A

PAPER

Cite this: J. Mater. Chem. A, 2016, 4, 11516

# Layer-by-layer assembly of exfoliated layered double hydroxide nanosheets for enhanced electrochemical oxidation of water†

Cong Zhang,‡[a] Jingwen Zhao,‡[b] Lei Zhou,[a] Zhenhua Li,[a] Mingfei Shao*[a] and Min Wei*[a]

How to develop cost-effective electrocatalysts for the oxygen evolution reaction (OER) is one of the critical issues in renewable energy storage and conversion technology. Here, we report the preparation of well-ordered ultrathin film (UTF) electrodes based on layered double hydroxide nanosheets (LDH NSs) and iron porphyrin (Fe-PP) through an electrostatic layer-by-layer (LBL) technique, which show excellent OER performance. By virtue of the high catalytic activity of LDH NSs and good electron-transfer ability of Fe-PP, the resulting CoNi-LDH NS/Fe-PP UTF exhibits a remarkably low overpotential (264 mV) to attain an OER current density of 10 mA $cm^{-2}$ and a substantially decreased Tafel slope of 37.6 mV $dec^{-1}$, much superior to that of the $IrO_2$ catalyst. Moreover, this method can be extended to the preparation of other UTFs based on LDHs and Fe-PP (*e.g.*, CoMn-LDH NS/Fe-PP, CoFe-LDH NS/Fe-PP and ZnCo-LDH NS/Fe-PP) with significantly enhanced OER performance relative to pristine LDH NSs. To illustrate the advantage of these UTFs in practical water splitting, a prototype electrolyzer cell is also fabricated by using the $(CoNi\text{-}LDH/Fe\text{-}PP)_{30}$ UTF as the anode and Pt wire as the cathode, which achieves the production of both oxygen and hydrogen by using a 1.5 V AA battery as the power source.

Received 26th March 2016
Accepted 28th June 2016

DOI: 10.1039/c6ta02537d

www.rsc.org/MaterialsA

## Introduction

Increasing energy demands have stimulated intense research on energy storage and conversion systems with high efficiency, low cost and environmental benignity. The oxygen evolution reaction (OER) in particular is an effective process to produce and store renewable energy, which is closely related to various promising energy systems including water splitting, solar cells, and metal–air batteries.[1–3] However, in practice, the kinetics of the OER are largely limited by its multistep proton-coupled electron transfer process; an efficient electrocatalyst is therefore particularly needed to expedite the reaction kinetics and reduce the energy consumption. Recently, noble metal-based materials (*e.g.*, $IrO_2$ and $RuO_2$) have shown rather high catalytic activity for the OER,[4,5] but suffer from their scarcity, high cost and poor stability in practical applications. To address these issues, increasing efforts have been focused on the high-efficiency and earth-abundant alternatives, such as first-row transition metal oxides/hydroxides and perovskites.[6–10]

Layered double hydroxides (LDHs) are a family of anionic layered materials, which consist of brucite-like $[Mg(OH)_2]$ host sheets with edge-sharing metal-$O_6$ octahedra.[11] The facile tunability of metal ions without altering the structure as well as the anion exchange properties of LDHs make them interesting alternatives for applications in electrochemical energy storage and conversion.[12,13] For instance, NiFe-LDH has been intensely investigated as an efficient OER catalyst owing to its high activity and stability in basic media;[14,15] and various strategies have been developed to further improve its performance either by hybridizing it with carbon materials (*e.g.*, carbon nanotubes (CNTs), graphene and carbon quantum dots (CQDs))[16–24] or by constructing nanostructures.[25–28] Recently, Hu *et al.* demonstrated that exfoliated LDH nanosheets (NSs) show a significantly enhanced performance compared with their bulk phase due to their improved intrinsic catalytic activity and conductivity.[14] However, exfoliated LDH NSs usually tend to aggregate owing to their extremely high surface energy, which thereby decreases the active site exposure and the charge mobility. On the other hand, the application of LDH NSs as electroactive materials for the OER is also restricted due to the charge transfer limitation between LDHs and the electrode. It is therefore desirable to employ a conductive mediator to uniformly disperse LDH NSs, which not only eliminates the agglomeration of electroactive sites, but facilitates electron

[a]State Key Laboratory of Chemical Resource Engineering, Beijing University of Chemical Technology, Beijing 100029, P. R. China. E-mail: shaomf@mail.buct.edu.cn; weimin@mail.buct.edu.cn; Fax: +86-10-64425385; Tel: +86-10-64412131

[b]Qingdao Industrial Energy Storage Research Institute, Qingdao Institute of Bioenergy and Bioprocess Technology, Chinese Academy of Science, Qingdao 266101, P. R. China

† Electronic supplementary information (ESI) available. See DOI: 10.1039/c6ta02537d

‡ Contributed equally to this work.

transfer between the electroactive species and the underlying electrode.

Iron porphyrin (Fe-PP), with extensive 2D 18 p-electrons, is an effective electron-transfer mediator,[29,30] which would be an encouraging candidate to accelerate the charge transfer between LDH NSs and the electrode. This inspires us to challenge the goal of fabricating OER electrodes *via* alternate layer-by-layer (LBL) assembly of positively charged LDH NSs and negatively charged Fe-PP. Herein, we demonstrate the fabrication of LDH NS/Fe-PP ultrathin films (UTFs), which give largely enhanced electrocatalytic water oxidation performance. The obtained UTFs show a long-range ordered structure with precisely controlled thickness and uniformity. The Fe-PP molecule not only serves as a dispersion reagent for LDH NSs, but also as an efficient mediator for facilitating the electron transfer of the UTF-based electrode. Based on the high activity of well-distributed LDH NSs and the enhanced electron transport arising from the Fe-PP molecules, the as-obtained $(CoNi\text{-}LDH/Fe\text{-}PP)_{30}$ UTF modified electrode exhibits a remarkably high current density of 30.8 mA $cm^{-2}$ at an overpotential of 300 mV, which is nearly six- and three-fold that of pristine CoNi-LDH NSs and the $IrO_2$ catalyst, respectively. Therefore, this work provides a feasible route for the construction of molecular-scale UTF catalysts toward the OER, which can be potentially used in electrochemical energy storage/conversion systems.

## Experimental section

### Reagents and materials

Ferriprotoporphyrin IX chloride (Fe-PP), formamide, and acetonitrile were purchased from Aladdin. $CoCl_2\cdot 6H_2O$, $NiCl_2\cdot 6H_2O$, $Fe(NO_3)_3\cdot 9H_2O$, $Zn(NO_3)_2\cdot 6H_2O$, $Mn(NO_3)_2$ solution (50 wt%), bromine, urea, hexamethylenetetramine (HMT), NaOH, and $NaNO_3$ were of analytical grade and used without further purification.

### Preparation of LDH precursors

CoNi-LDH–$NO_3$ was synthesized by using a hydrothermal method reported previously.[11] Briefly, 5.0 mM $CoCl_2\cdot 6H_2O$, 2.5 mM $NiCl_2\cdot 6H_2O$ and 45 mM HMT were dissolved in a 1000 mL three-necked flask with deionized Milli-Q water. The resulting solution was refluxed for 6 h under a nitrogen atmosphere and continuous stirring. A pink brucite-like precipitate (CoNi–hydroxide) was obtained by centrifugation, washed with deionized water and anhydrous ethanol in turn, and dried at room temperature. Subsequently, the CoNi–hydroxide (0.186 g) was dispersed in 100 mL of anhydrous acetonitrile (99.8%) containing 7.0 mM of bromine. The mixture was sealed in an airtight capped flask and stirred for 24 h in the dark. A green yellow product, identified as the $Br^-$ intercalated CoNi-LDH phase, was collected by centrifugation and washed thoroughly with anhydrous ethanol. To prepare the nitrate intercalated CoNi-LDH, the as-prepared 0.25 g CoNi-LDH–Br sample was further added into a flask containing 1.5 M $NaNO_3$ into 200 mL of ethanol/water binary liquid (1 : 1, v/v). The flask was mechanically shaken at room temperature in a nitrogen atmosphere for 48 h. The product was centrifuged, washed with anhydrous ethanol, and air-dried. The exfoliation was performed as follows: 0.05 g of CoNi-LDH–$NO_3$ was dispersed in 100 mL of formamide in a flask sealed in a nitrogen atmosphere, and then agitated for 60 h, giving a colloidal suspension. The resulting translucent colloidal solution was further centrifuged to remove possible unexfoliated LDH particles. The final colloidal suspension of CoNi-LDH NSs was stored in a refrigerator.

### Fabrication of LDH/Fe-PP UTFs

Indium-tin-oxide (ITO) glass substrates (1 × 3 cm, 10 Ω per square) were cleaned in an ultrasonic bath using the following reagents in sequence: water, acetone, ethanol and water for 10 min. After the cleaning procedure, the surfaces of the substrates became hydrophilic and negatively charged. The substrates were stored in deionized water before use. Multilayer films composed of CoNi-LDH NSs and Fe-PP molecules were fabricated on a pretreated ITO substrate through the LBL technique. The ITO glass substrate was dipped into a colloidal suspension of CoNi-LDH NSs (0.5 g $L^{-1}$) for 10 min and washed thoroughly with deionized water. Then it was immersed into an aqueous solution of Fe-PP (1.0 g $L^{-1}$) for another 10 min and rinsed with water. Subsequently, the deposition operation for CoNi-LDH NSs and Fe-PP was repeated $n$ times to obtain $(CoNi\text{-}LDH/Fe\text{-}PP)_n$ UTFs with LDH NSs as the terminal end. The resulting $(CoNi\text{-}LDH/Fe\text{-}PP)_n$ UTFs on the ITO substrate were dried in a vacuum oven at ambient temperature.

### Structural characterization

Powder X-ray diffraction patterns of the LDH samples were collected on a Shimadzu XRD-6000 diffractometer using a Cu Kα source. The UV-vis spectra were collected with a Shimadzu U-3000 spectrophotometer. The morphology of the UTFs was investigated by using a scanning electron microscope (SEM; Zeiss SUPRA 55) with an accelerating voltage of 20 kV, combined with energy-dispersive X-ray spectroscopy (EDX) for the determination of the metal composition. AFM was performed on a Veeco Nano Scope IIIA AFM instrument (Digital instruments, Santa Barbara, CA, USA) in the tapping mode. X-ray photoelectron spectra (XPS) were recorded on a Thermo VG Escalab 250 X-ray photoelectron spectrometer at a pressure of about $2 \times 10^{-9}$ Pa with Al Kα X-rays as the excitation source. Raman measurements were carried out with 633 nm excitation by using a confocal Raman microspectrometer (Renishaw, in Via-Reflex, 633 nm).

### Electrochemical measurements

Electrochemical studies were carried out in a standard three electrode system controlled by a CHI 660E electrochemical workstation (Shanghai Chenhua Instrument Co., China). The $(CoNi\text{-}LDH/Fe\text{-}PP)_n$ UTFs were used as the working electrodes, a platinum wire as the counter electrode and an Ag/AgCl electrode as the reference electrode. The scan rate was 50 mV $s^{-1}$ for cyclic voltammetry (CV) measurements and 5 mV $s^{-1}$ for linear sweep voltammetry (LSV) curves. Tafel plots were plotted from

the corresponding LSV polarization curves. The electrochemically active surface area (EASA) was determined by measuring the capacitive current associated with double-layer charging from the scan-rate dependence of CVs. For this measurement, the potential window of CVs was 0.2–0.3 V *vs.* Ag/AgCl; the scan rates were 20, 40, 60, 80, 100 and 120 mV $s^{-1}$. The double layer capacitance ($C_{dl}$) was estimated by plotting the $\Delta j = (j_a - j_c)$ at 0.25 V *vs.* Ag/AgCl against the scan rates. The linear slope is twice the double layer capacitance $C_{dl}$, which can be used to represent the electrochemically active surface area. The apparent turnover frequency (TOF) value was calculated from the equation: TOF $= j \times A/(4F \times m)$, where $j$ is the current density at a given overpotential (*e.g.*, $\eta = 300$ mV); $A$ is the surface area of the electrode; $F$ is the Faraday constant (a value of 96 485 C $mol^{-1}$), and $m$ is the mole number of metal on the electrode. This TOF is estimated by assuming that all the electroactive metal atoms in the LDH NS/Fe-PP UTF modified electrode are catalytically active for the OER.[14,16,17,20] The electrolysis experiment of the faradaic efficiency test was performed in an airtight H shaped cell. The platinum counter electrode was placed on one side of the cell; the modified working electrode, an Ag/AgCl reference electrode and a magnetic stirring bar were placed on the other side. The cell was purged with nitrogen for 20 min before the OER measurement. A constant oxidation current of 100 mA was continued for ~600 s. The faradaic yield was calculated from the total amount of charge $Q$ (C) passed through the cell and the total amount of oxygen produced ($n_{O_2}$: mmol). Assuming that four electrons are needed to produce one $O_2$ molecule, the faradaic efficiency is calculated as follows: faradaic efficiency $= 4F \times n_{O_2}/Q = 4F \times n_{O_2} \times 10/t$, where $F$ is the Faraday constant; $Q = t \times 0.1$ (C) and $t$ is the time (s) for the constant oxidation current. The total amount of oxygen produced was measured using a drainage method.[26,31]

## Results and discussion

### Morphology and structure of the (CoNi-LDH/Fe-PP)$_n$ UTFs

The CoNi-LDH NSs (with a lateral size of ~2 μm) were prepared as reported previously,[11] serving as positively charged building blocks to assemble with negatively charged Fe-PP (Fig. S1 and S2†). The (CoNi-LDH/Fe-PP)$_n$ UTFs were fabricated by alternate assembly of CoNi-LDH NSs with Fe-PP by the LBL method (Fig. 1a). The assembly process was monitored by using UV-vis spectra (Fig. 1b: the bilayer number $n$ varies from 2 to 12). The (CoNi-LDH/Fe-PP)$_n$ UTFs exhibit a strong absorption band at 402.9 nm attributed to the characteristic Q band of Fe-PP, and the intensity correlates linearly with the increase of bilayer number $n$, indicative of a stepwise and regular deposition procedure with an almost equal amount of Fe-PP incorporated in each cycle. This LBL process is further confirmed by the visible color evolution with the increase of $n$ (Fig. S3†). The surface morphology and thickness of (CoNi-LDH/Fe-PP)$_n$ UTFs with different bilayers are investigated by SEM and AFM. A top-view SEM image of the (CoNi-LDH/Fe-PP)$_{10}$ UTF shows a continuous and uniform film surface with apparent flat LDH NSs (Fig. 2a); the AFM topographical image further demonstrates a smooth surface with a root-mean-square roughness of 8.703 nm (Fig. 2b). The side-view SEM images with different bilayers display an increasing thickness of 10 nm, 16 nm and 22 nm for (CoNi-LDH/Fe-PP)$_n$ UTFs ($n$ = 4, 8 and 12, respectively; Fig. 2c–e), corresponding to an average increment of ~2 nm per bilayer. The XRD patterns (Fig. S4a†) of the multilayer films illustrate the evolution of a Bragg peak at $2\theta$ 4.4° ($d_{001}$ = 2.01 nm), which is attributed to a superlattice reflection of the periodic layered structure of UTFs. The reflection intensity enhances progressively along with the increase of the bilayer number from 4 to 30, confirming the successful fabrication of the (CoNi-LDH/Fe-PP)$_n$ UTFs. Moreover, the crystallographic thickness of an exfoliated CoNi-LDH nanosheet is determined to be ~0.57 nm by AFM (Fig. S4b†), consistent with a single LDH monolayer (~0.48 nm).[32] Accordingly, the interlayer height for the UTFs is evaluated to be ~1.44 nm, which is in accordance with the size of the Fe-PP molecule (1.42 nm). The energy dispersive X-ray spectroscopy (EDX) mapping analysis (Fig. S5†) of the (CoNi-LDH/Fe-PP)$_{10}$ UTF shows that Co, Ni, Fe and O are homogeneously distributed throughout the film with a Co/Ni/Fe ratio of 4/2/1 (Table S1†), consistent with the XPS results (Fig. S6†). Raman spectra of (CoNi-LDH/Fe-PP)$_n$ UTFs (Fig. S7 and Table S2†) display both the characteristic peaks of Fe-PP molecules (1120 $cm^{-1}$, 1217 $cm^{-1}$, 1363 $cm^{-1}$, 1560 $cm^{-1}$ and 1618 $cm^{-1}$) and the LDH phase (180 $cm^{-1}$, 1060 $cm^{-1}$ and 1373 $cm^{-1}$).

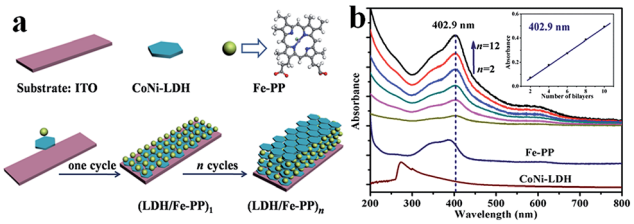


Fig. 1 (a) Schematic representation of the LBL assembly of the (CoNi-LDH/Fe-PP)$_n$ UTFs. (b) UV-vis spectra of the (CoNi-LDH/Fe-PP)$_n$ UTFs ($n$ = 2–12) on a quartz glass substrate (inset: the linear relationship between absorbance at 403 nm and bilayer number $n$).

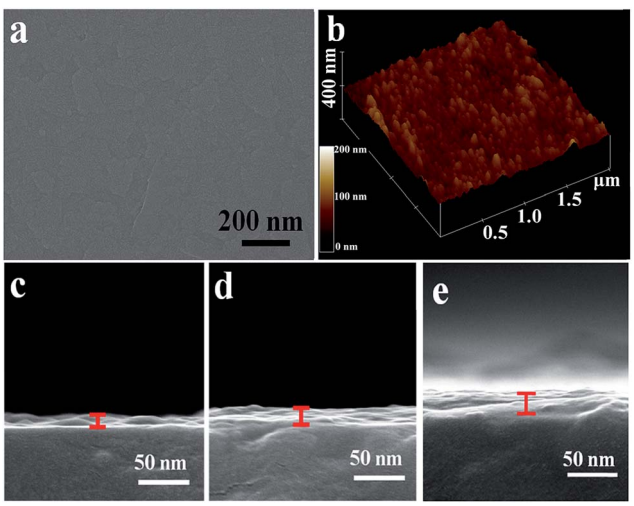


Fig. 2 Morphology of the (CoNi-LDH/Fe-PP)$_n$ UTFs: (a) top-view SEM image for $n$ = 10; (b) tapping-mode AFM image for $n$ = 10; side view SEM images for (c) $n$ = 4, (d) $n$ = 8, and (e) $n$ = 12.

### OER electrocatalytic performance

The OER activity of $(CoNi\text{-}LDH/Fe\text{-}PP)_n$ UTFs was evaluated in 1.0 M KOH using a standard three-electrode system. Four control samples were used for a comparison study: CoNi-LDH NS/Fe-PP mixture (denoted as CoNi-LDH/Fe-PP-M/ITO), CoNi-LDH NS/ITO, Fe-PP/ITO and ITO substrate (see ESI† for the detailed preparation). The LSV curves (Fig. 3a) show that both ITO substrate and Fe-PP do not display any catalytic activity toward the OER. The CoNi-LDH/Fe-PP-LBL UTF displays the lowest onset potential (~230 mV) and the largest current density at the same overpotential ($\eta$) among these electrodes, revealing the highest OER activity. To reach $j = 10$ mA cm$^{-2}$, the as-prepared CoNi-LDH/Fe-PP-LBL requires a potential of 264 mV (Fig. 3a, inset), which is 50 mV and 69 mV less than that of CoNi-LDH/Fe-PP-M and CoNi-LDH, respectively. The current density at $\eta$ = 300 mV is 30.8 mA cm$^{-2}$ for CoNi-LDH/Fe-PP-LBL, which is ~4.8 and 6.4 times larger than that for CoNi-LDH/Fe-PP-M and CoNi-LDH electrodes, respectively. To confirm that the oxidation currents were associated with water oxidation, the actual oxygen production catalyzed by the CoNi-LDH/Fe-PP-LBL UTF at a constant current of 100 mA cm$^{-2}$ was obtained by using a simple drainage method in an air-tight reactor to measure the faradaic yield of $O_2$ formation (Fig. S8†). The UTF shows a faradaic efficiency of 99.8% after an induction period of 20 min, indicating a satisfactory energy conversion from electrical energy to chemical energy. Moreover, the Tafel slope of CoNi-LDH/Fe-PP-LBL which was plotted from the corresponding OER polarization curves is 37.6 mV dec$^{-1}$ (Fig. 3b), much smaller than that of CoNi-LDH/Fe-PP-M (53.7 mV dec$^{-1}$) and CoNi-LDH (67.2 mV dec$^{-1}$), indicating the superior OER performance of CoNi-LDH/Fe-PP-LBL. It is worth mentioning that the Tafel slope (37.6 dec$^{-1}$) is among those reported for the most kinetically active OER catalysts for the water-splitting process (Fig. S9†). In addition, electrochemical impedance spectroscopy (EIS, Fig. 3c) results show that the CoNi-LDH/Fe-PP-LBL electrode possesses the smallest charge transfer resistance among the three samples, implying the advantage of ordered UTFs for charge transfer. The EASAs of the three samples were calculated by using the $C_{dl}$.[31] It is found that CoNi-LDH/Fe-PP-LBL gives a value of 0.04 F cm$^{-2}$, which is 3.4 times and 4.2 times larger than that of CoNi-LDH/Fe-PP-M and CoNi-LDH, respectively (Fig. S10†). Because of the extremely high surface energy of LDH NSs, the LDH materials dropped on the electrode show a totally different morphology, which causes serious aggregation between particles (Fig. S11†). The resulting increased resistance and decreased EASA for the as-obtained drop electrodes limit their electrocatalytic activity. The results above indicate that the ordered stacking of LDH NSs and Fe-PP molecules in CoNi-LDH/Fe-PP-LBL UTFs contributes to the enhanced OER performance. To further demonstrate the superiority of Fe-PP as an electron-transfer mediator in UTFs, two other control samples of CoNi-LDH/$CO_3^{2-}$-LBL UTFs and CoNi-LDH/$NO_3^-$-LBL UTFs were prepared (see ESI† for the detailed preparation process). Although these two UTFs exhibit fairly good OER performance, their current densities (6.81 and 3.43 mA cm$^{-2}$ for the CoNi-LDH/$CO_3^{2-}$-LBL UTF and CoNi-LDH/$NO_3^-$-LBL UTF, respectively) at $\eta$ = 300 mV are obviously lower than that of CoNi-LDH/Fe-PP-LBL UTFs (Fig. S12a†). The CoNi-LDH/PSS UTF and CoNi-LDH/SDS UTF were also prepared (see ESI† for the detailed preparation process) as control samples. Although the large size of PSS and SDS in the interlayer region of LDH NSs could provide sufficient space for the water oxidation reaction, these two UTFs show obviously lower current densities (9.74 and 4.70 mA cm$^{-2}$, respectively) at $\eta$ = 300 mV compared with the CoNi-LDH/Fe-PP UTF (Fig. S12b†). The above results indicate that the conductive Fe-PP molecules in the interlayer region significantly promote the OER performance of LDHs. The superiority of the CoNi-LDH/Fe-PP UTF toward the OER is also illustrated by the smaller resistance and Tafel slope relative to the CoNi-LDH/PSS-LBL UTF and CoNi-LDH/SDS-LBL UTF (Fig. S12c and d†). Therefore, Fe-PP in the UTF not only provides a sufficient interlayer space, but also acts as an electron transfer mediator to accelerate the water oxidation reaction.

To further reveal the OER performance of UTFs as a function of film thickness, a series of $(CoNi\text{-}LDH/Fe\text{-}PP)_n$ UTFs with different bilayers were fabricated and their electrocatalytic activities toward the OER were studied. As shown in Fig. 3d, the

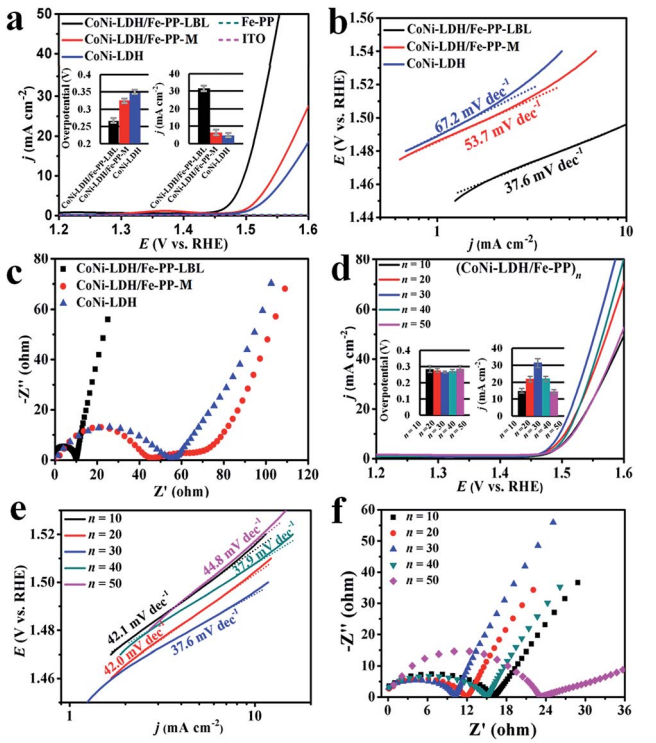


Fig. 3 (a) LSV curves of CoNi-LDH/Fe-PP-LBL, CoNi-LDH/Fe-PP-drop and CoNi-LDH-drop (inset: overpotentials required for $j = 10$ mA cm$^{-2}$ and current densities at $\eta$ = 300 mV). (b) Tafel slopes and (c) EIS curves of CoNi-LDH/Fe-PP-LBL, CoNi-LDH/Fe-PP-drop and CoNi-LDH-drop. (d) LSV curves of $(CoNi\text{-}LDH/Fe\text{-}PP)_n$ UTFs with different bilayer numbers ($n$ = 10–50; inset: overpotentials required for $j = 10$ mA cm$^{-2}$ and current densities at $\eta$ = 300 mV). (e) Tafel slopes and (f) EIS curves of $(CoNi\text{-}LDH/Fe\text{-}PP)_n$ UTFs with different bilayers numbers ($n$ = 10–50). The error bar represents the results from five independent measurements: the OER performance of UTFs is highly reproducible under the same conditions.

onset potential first decreases from 1.47 to 1.46 with the increase of bilayer number ($n$) from 10 to 30, while increases significantly with further enhancement of $n$. The overpotential of $(CoNi\text{-}LDH/Fe\text{-}PP)_n$ UTFs ($n$ = 10–50) at $j = 10$ mA cm$^{-2}$ also shows a similar trend: the $(CoNi\text{-}LDH/Fe\text{-}PP)_{30}$ UTF gives the smallest overpotential (264 mV). Fig. 3e illustrates the Tafel plots derived from polarization curves of these UTFs, from which the Tafel slopes are 42.1, 42.0, 37.6, 37.9 and 44.8 mV dec$^{-1}$ for $n$ = 10, 20, 30, 40 and 50, respectively. It is clear that the $(CoNi\text{-}LDH/Fe\text{-}PP)_{30}$ UTF exhibits the smallest Tafel slope. In addition, Fig. 3f shows the typical EIS for the $(CoNi\text{-}LDH/Fe\text{-}PP)_n$ UTF modified electrode in 1.0 M KOH solution. The diameter of the semicircle part decreases significantly as the bilayer number increases from 10 to 30; while it starts to increase with a further increase of $n$ from 30 to 50. The smallest charge transfer resistance is present in the $(CoNi\text{-}LDH/Fe\text{-}PP)_{30}$ UTF electrode. The results demonstrate that a suitable thickness ($n$ = 30) can effectively enhance OER activity; while an excess packing of active components would hinder electron transfer and mass diffusion.

In order to further testify the preparation generality of LDH NS/Fe-PP UTFs, various LDH NS (CoMn-, CoFe- and ZnCo-LDH) based UTFs were fabricated by using the electrostatic LBL assembly technique. The related characterization and discussion about synthesized LDHs have been provided in the ESI (Fig. S13 and S14†). The optimal UTF thickness of various binary LDHs for OER performance is found to be 30, 20, and 30 for CoMn-, CoFe and ZnCo-LDH NS/Fe-PP UTFs, respectively (Fig. S15†). Compared with their pristine LDH NS modified electrodes, the OER performance of all these LDH NS/Fe-PP UTFs is significantly improved with a lower onset potential, larger current density, smaller overpotential and Tafel slope (Fig. 4). For instance, the current densities (at $\eta$ = 300 mV) for CoNi-, CoMn-, CoFe- and ZnCo-LDH NSs enhance by 6.4-, 3.2-, 1.7- and 2.4-fold after LBL assembly with Fe-PP, respectively (Fig. 4c). It is worth noting that the $(CoNi\text{-}LDH/Fe\text{-}PP)_{30}$ UTF exhibits superior activity among all these UTF samples. In addition, the intrinsic activity of the LDH NS/FePP UTFs was further studied by using their apparent TOFs, which give 0.029, 0.009, 0.006 and 0.002 s$^{-1}$ (Fig. 4e) for CoNi-, CoMn-, CoFe- and ZnCo-LDH NS/Fe-PP UTFs, respectively, much larger than that of corresponding pristine LDH NSs.

The XPS analysis was conducted to better understand the interaction between CoNi-LDH NSs and Fe-PP molecules. The Co 2p core lines of the pristine CoNi-LDH NSs split into Co $2p_{3/2}$ (781.9 eV) and Co $2p_{1/2}$ (797.8 eV) peaks accompanied by two satellite bands at 786.5 and 803.0 eV (Fig. 5a). After binding with Fe-PP molecules, both Co $2p_{3/2}$ and Co $2p_{1/2}$ shift to a lower energy region (781.4 and 797.3 eV, respectively), along with a slight decrease in the satellite bands. Such a clear shift in binding energy indicates a partial valence change from $Co^{2+}$ to $Co^{3+}$. More information is given in the corresponding deconvolution of the Co 2p spectra (Fig. 5b). The $Co^{3+}$-to-$Co^{2+}$ ratio of CoNi-LDH NSs calculated from the integral peak area increases significantly from 1.14 to 1.36 after coupling with Fe-PP. The Ni $2p_{3/2}$ (856.8 eV) and Ni $2p_{1/2}$ (875.1 eV) peaks accompanied by two satellite bands confirm the existence of the $Ni^{2+}$ state in

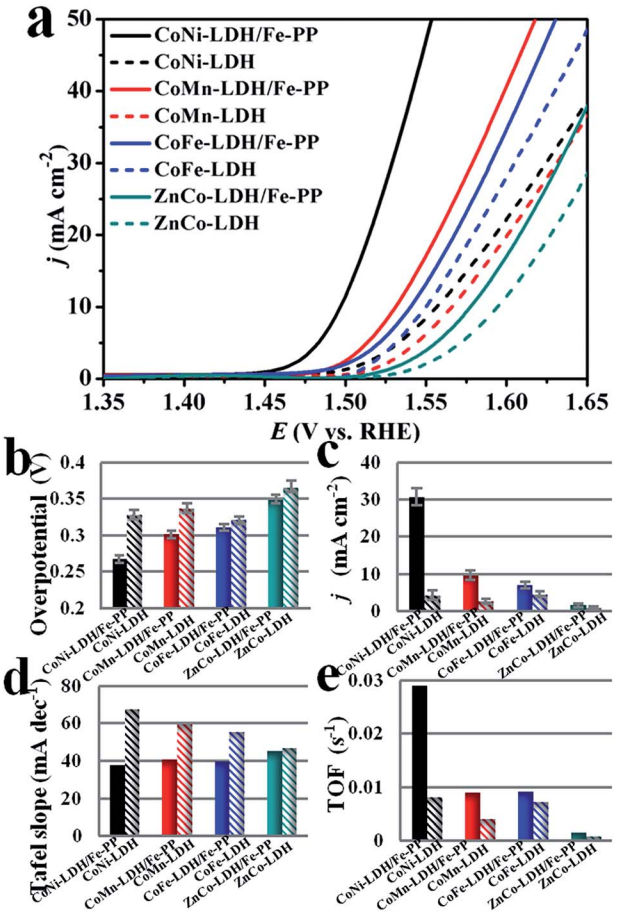


Fig. 4 (a) LSV curves, (b) overpotentials required for $j$ = 10 mA cm$^{-2}$, (c) current densities at $\eta$ = 300 mV, (d) Tafel slopes and (e) TOF values calculated from current densities at $\eta$ = 300 mV for various LDHs and corresponding $(LDH\text{-}NS/Fe\text{-}PP)_{30}$ UTFs.

pristine CoNi-LDH (Fig. 5c). A 0.4 eV shift to higher binding energy is observed for the $(CoNi\text{-}LDH/Fe\text{-}PP)_{30}$ UTF sample, indicating a decrease in the electron density of Ni. In the case of Fe-PP, no clear shift of Fe $2p_{3/2}$ (710.5 eV) and Fe $2p_{1/2}$ (723.8 eV) is found in Fe-PP and CoNi-LDH/Fe-PP (Fig. 5d); however, N 1s (Fig. 5e) and O 1s (Fig. 5f) respectively show an ~0.38 eV and ~0.61 eV decrease for the CoNi-LDH/Fe-PP sample compared with pristine Fe-PP. As a result, both the binding energy shifts of Co, Ni and N, O indicate electron transfer from the transition metal in CoNi-LDH NSs to the conjugate ring of Fe-PP. Moreover, protoporphyrin IX (PP) was used to prepare the CoNi-LDH/PP-LBL UTF as a control sample to understand the role of ligating atom Fe in porphyrin. Notably, the $(CoNi\text{-}LDH/Fe\text{-}PP)_{30}$ UTF presents a 10 mV lower onset potential and a 2.3-fold higher current density than the $(CoNi\text{-}LDH/PP)_{30}$ UTF at $\eta$ = 300 mV, confirming the enhanced intrinsic electrocatalytic activity of the $(CoNi\text{-}LDH/Fe\text{-}PP)_{30}$ UTF (Fig. S16†). The EIS result illustrates that the $(CoNi\text{-}LDH/Fe\text{-}PP)_{30}$ UTF holds a much lower charge transfer resistance and a larger ion diffusion capacity than the $(CoNi\text{-}LDH/PP)_{30}$ UTF. This suggests that the ligating atom Fe plays a positive role in improving the conductivity of the electron transfer mediator (Fe-PP).

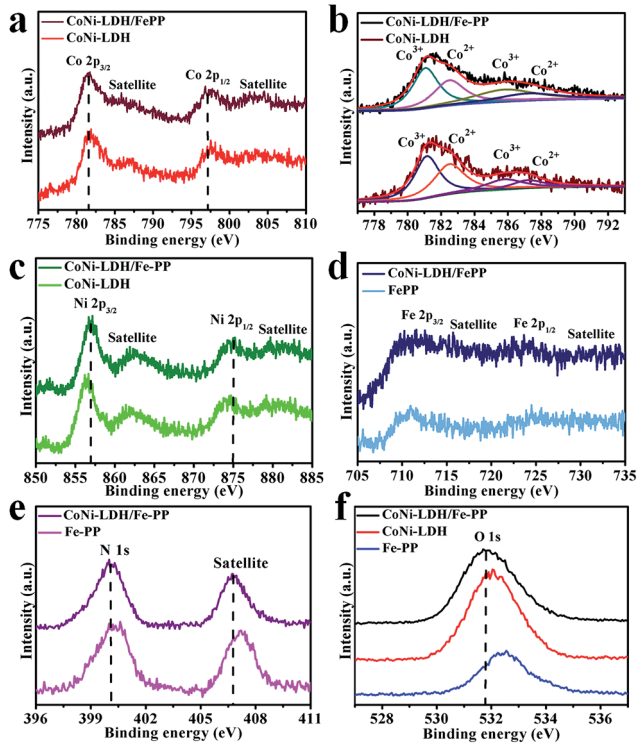


Fig. 5 (a) Typical Co 2p, (b) deconvoluted Co 2p, and (c) Ni 2p XPS spectra of the $(CoNi\text{-}LDH/Fe\text{-}PP)_{30}$ UTF and pure CoNi-LDH. (d) Typical Fe 2p and (e) N 1s XPS spectra of the $(CoNi\text{-}LDH/Fe\text{-}PP)_{30}$ UTF and pure Fe-PP. (f) Typical O 1s XPS spectra of the $(CoNi\text{-}LDH/Fe\text{-}PP)_{30}$ UTF, pure CoNi-LDH and pure Fe-PP.

To elucidate the intrinsic active site of CoNi-LDH UTFs, we investigated the redox behaviour of various CoNi-LDH/Fe-PP UTFs with different Co/Ni molar ratios. The CoNi-LDH NSs exhibit a high current density of the redox peak, which is nearly 40-fold larger than that of the Fe-PP molecule (Fig. S17a,† inset), further indicating that the active sites for the OER are derived from LDH NSs. Representative CV curves reveal that all these CoNi-LDH/Fe-PP UTFs exhibit broad redox peaks (Fig. S17a†), which can be attributed to the pseudocapacitive processes of $Co^{2+}/Co^{3+}$, $Ni^{2+}/Ni^{3+}$ and $Co^{3+}/Co^{4+}$ with the assistance of $OH^-$:[33]

$$Co(OH)_2 + OH^- \rightarrow CoOOH + H_2O + e^- \quad (1)$$

$$Ni(OH)_2 + OH^- \rightarrow NiOOH + H_2O + e^- \quad (2)$$

$$CoOOH + OH^- \rightarrow CoO_2 + H_2O + e^- \quad (3)$$

It is found that the anodic peak tends to appear at a high potential (~1.39 V) with a low content of Co in $CoNi_2$-LDH/Fe-PP, along with a high OER onset potential (~1.54 V). With the increase of the Co/Ni molar ratio to 1 : 1, the anodic peak shifts to a lower potential (~1.36 V), and the corresponding OER onset potential is at ~1.53 V. A further enhancement of the Co content $Co_2Ni$-LDH/Fe-PP results in a decreased OER onset potential of ~1.52 V. The improved OER electrocatalytic activity with a high Co content implies that Co serves as the active site toward the OER. It is reported that $Co^{3+}$ plays an important role in the OER performance of Co-based catalysts, which transforms to $Co^{4+}$ easily before achieving water oxidation to $O_2$.[34–38] To test whether $Co^{3+}$ is more beneficial to the OER in CoNi-LDH/Fe-PP UTFs, CoNi-LDHs with various $Co^{3+}$ content were obtained by tuning the quantity of the oxidizing agent ($Br_2$, for the detailed preparation process, see ESI†). Consequently, the $Co^{3+}/Co^{4+}$ redox peaks become more obvious as the $Co^{3+}$ content increases in the $(CoNi\text{-}LDH/Fe\text{-}PP)_{30}$ UTF (Fig. S17b†). Moreover, the overpotential of the OER current decreases gradually with the increase of $Co^{3+}$ content, indicating that $Co^{3+}$ plays an indispensible role in OER performance.

Given the discussions above and previous studies,[39–41] the catalytic process of $(CoNi\text{-}LDH/Fe\text{-}PP)_n$ UTFs toward the OER is proposed and shown in Scheme S1.† Fe-PP molecules act as electron acceptors, giving rise to more positively charged Co species in CoNi-LDH NSs (Scheme S1-I†). The reaction begins with the adsorption and discharge of the $OH^-$ anion at the surface of positively charged LDH NSs to form adsorbed OH species, which will be translated to adsorbed OOH species afterwards (Schemes S1-II and III†). The adsorbed OOH species then undergo a reaction with additional $OH^-$ which is catalysed by LDH NSs, resulting in the formation of adsorbed $O_2$ (Scheme S1-IV†). The desorption of $O_2$ occurs in the last step, along with the recovery of CoNi-LDH to its initial state. These $(CoNi\text{-}LDH/Fe\text{-}PP)_n$ UTFs offer several advantages for the OER: (1) the LDH NSs with ordered arrangement and good dispersion display a high OER performance *via* fully exposed active sites; (2) Fe-PP between adjacent LDH NSs serves as a conducting pathway to enhance charge transfer in the catalytic reaction; (3) the electrostatic interaction between LDH NSs and Fe-PP enhances the $Co^{3+}$ content and the resulting improved OER activity.

We further investigated the OER performance of the $(CoNi\text{-}LDH/Fe\text{-}PP)_{30}$ UTF by comparing with that of the $IrO_2$ catalyst (0.14 mg $cm^{-2}$: the same mass loading of the catalyst as that of the $(CoNi\text{-}LDH/Fe\text{-}PP)_{30}$ UTF based on noble metal Ir). The $(CoNi\text{-}LDH/Fe\text{-}PP)_{30}$ UTF affords a nearly three-fold larger current density than that of the $IrO_2$ catalyst. An overpotential of ~1.49 V is required to achieve 10 mA $cm^{-2}$ for the UTF, smaller than that of the $IrO_2$ catalyst (~1.53 V, Fig. 6a). Moreover, the $(CoNi\text{-}LDH/Fe\text{-}PP)_{30}$ UTF also exhibits an excellent durability in alkaline solutions. When operating the OER at $\eta = 300$ mV, the $(CoNi\text{-}LDH/Fe\text{-}PP)_{30}$ UTF shows a nearly constant current density (maintaining 98.2% of the initial current density) during the 20 000 s continuous test. In contrast, the current density of the $IrO_2$ catalyst only maintains 83.7% of the initial current density (Fig. 6b). The LSV curve of the $(CoNi\text{-}LDH/Fe\text{-}PP)_{30}$ UTF after the 20 000 s OER test (at a potential of 1.53 V) overlaps with that of the fresh UTF (Fig. S18†). Furthermore, no obvious change in its surface morphology is observed (Fig. S19†); UV-vis absorption spectra do not show significant loss of Fe-PP during the durability test (Fig. S20†). The results indicate that the $(CoNi\text{-}LDH/Fe\text{-}PP)_{30}$ UTF possesses a strong tolerance against the surface tension of evolving oxygen bubbles, which can serve as a robust and durable electrocatalytic material toward the OER. To test the feasibility of $(LDH\ NS/Fe\text{-}PP)_n$ UTFs in practical water splitting, a prototype electrolyzer cell was fabricated (Fig. 6c). The $(CoNi\text{-}LDH/Fe\text{-}PP)_{30}$ UTF modified ITO glass was used as the anode, Pt wire as the

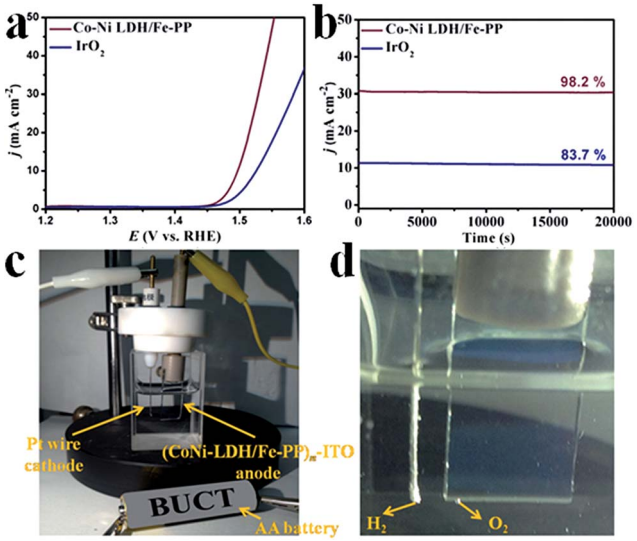


Fig. 6 (a) LSV curves of the $(CoNi\text{-}LDH/Fe\text{-}PP)_{30}$ UTF and the $IrO_2$ catalyst on the ITO electrode in 1 M KOH. (b) Chronoamperometric responses of the $(CoNi\text{-}LDH/Fe\text{-}PP)_{30}$ UTF and $IrO_2$ electrode at $\eta$ = 300 mV in 1 M KOH solution. (c) Water-splitting cell driven by a 1.5 V AA battery. (d) Cathode and anode of the water-splitting cell.

cathode, and a 1.5 V AA battery was used to power the cell. The evolution of both oxygen and hydrogen is clearly observed by using this water electrolysis cell (Fig. 6d); while water splitting cannot occur over the pristine ITO anode (Fig. S21†). More clear $H_2$ and $O_2$ bubbles can be observed on the surface of Pt wire and the $(CoNi\text{-}LDH/Fe\text{-}PP)_{30}$ UTF modified ITO substrate (Fig. S22†) when increasing the potential to 1.7 V (*vs.* RHE). Moreover, continuous bubble effusion is observed in both anode and cathode of the prototype electrolyzer cell for the 2 h test, indicating the durability of the $(CoNi\text{-}LDH/Fe\text{-}PP)_{30}$ UTF. Thus, a voltage of 1.5 V for water oxidation by using a non-precious catalyst is successfully achieved with an ultralow overpotential for water-splitting devices.

## Conclusion

In conclusion, we have fabricated UTF-based OER catalysts through a LBL assembly method by alternately stacking the positively charged LDH NSs with the negatively charged Fe-PP molecules. The as-obtained $(CoNi\text{-}LDH/Fe\text{-}PP)_{30}$ UTF exhibits an excellent OER performance, with a remarkably small onset potential of ~230 mV and Tafel slope of 37.6 mV $dec^{-1}$, much superior to the performance of pristine LDH NSs and the $IrO_2$ catalyst. Based on the high stability of the $(CoNi\text{-}LDH/Fe\text{-}PP)_{30}$ UTF, an efficient electrolyzer cell was demonstrated by using the $(CoNi\text{-}LDH/Fe\text{-}PP)_{30}$ UTF as the anode. It is expected that these LDH NS-based UTFs would show promising applications in electrochemical and photoelectron-chemical water splitting devices.

## Acknowledgements

This work was supported by the National Natural Science Foundation of China (NSFC), the 973 Program (Grant No. 2014CB932102), the Fundamental Research Funds for the Central Universities (buctrc201506; YS 1406) and the Specialized Research Fund for the Doctoral Program of Higher Education (20130010110013).

## Notes and references

1 T. C. Sum and N. Mathews, *Energy Environ. Sci.*, 2014, **7**, 2518.
2 Z. Wang, D. Xu, J. Xu and X. Zhang, *Chem. Soc. Rev.*, 2014, **43**, 7746.
3 K. Zeng and D. Zhang, *Prog. Energy Combust. Sci.*, 2010, **36**, 307.
4 K. S. Exner, J. Anton, T. Jacob and H. Over, *ChemElectroChem*, 2015, **2**, 707.
5 K. Sardar, S. C. Ball, J. D. B. Sharman, D. Thompsett, J. M. Fisher, R. A. P. Smith, P. K. Biswas, M. R. Lees, R. J. Kashtiban, J. Sloan and R. I. Walton, *Chem. Mater.*, 2012, **24**, 4192.
6 M. Gao, Y. Xu, J. Jiang, Y. Zheng and S. Yu, *J. Am. Chem. Soc.*, 2012, **134**, 2930.
7 Y. Liang, Y. Li, H. Wang, J. Zhou, J. Wang, T. Regier and H. Dai, *Nat. Mater.*, 2011, **10**, 780.
8 J. Suntivich, K. J. May, H. A. Gasteiger, J. B. Goodenough and Y. Shao-Horn, *Science*, 2011, **334**, 1383.
9 C. Qiao, Y. Zhang, Y. Zhu, C. Cao, X. Bao and J. Xu, *J. Mater. Chem. A*, 2015, **3**, 6878.
10 D. Tang, Y. Han, W. Ji, S. Qiao, X. Zhou, R. Liu, X. Han, H. Huang, Y. Liu and Z. Kang, *Dalton Trans.*, 2014, **43**, 15119.
11 J. Liang, R. Ma, N. Iyi, Y. Ebina, K. Takada and T. Sasaki, *Chem. Mater.*, 2010, **22**, 371.
12 M. Shao, R. Zhang, Z. Li, M. Wei, D. G. Evans and X. Duan, *Chem. Commun.*, 2015, **51**, 15880.
13 G. Fan, F. Li, D. G. Evans and X. Duan, *Chem. Soc. Rev.*, 2014, **43**, 7040.
14 F. Song and X. Hu, *Nat. Commun.*, 2014, **5**, 4477.
15 N. Han, F. Zhao and Y. Li, *J. Mater. Chem. A*, 2015, **3**, 16348.
16 M. Gong, Y. Li, H. Wang, Y. Liang, J. Z. Wu, J. Zhou, J. Wang, T. Regier, F. Wei and H. Dai, *J. Am. Chem. Soc.*, 2013, **135**, 8452.
17 X. Long, J. Li, S. Xiao, K. Yan, Z. Wang, H. Chen and S. Yang, *Angew. Chem.*, 2014, **53**, 7584.
18 C. Tang, H. S. Wang, H. F. Wang, Q. Zhang, G. L. Tian, J. Q. Nie and F. Wei, *Adv. Mater.*, 2015, **27**, 4516.
19 H. Wang, C. Tang and Q. Zhang, *J. Mater. Chem. A*, 2015, **3**, 16183.
20 W. Ma, R. Ma, C. Wang, J. Liang, X. Liu, K. Zhou and T. Sasaki, *ACS Nano*, 2015, **9**, 1977.
21 X. Yu, M. Zhang, W. Yuan and G. Shi, *J. Mater. Chem. A*, 2015, **3**, 6921.
22 D. H. Youn, Y. B. Park, J. Y. Kim, G. Magesh, Y. J. Jang and J. S. Lee, *J. Power Sources*, 2015, **294**, 437.
23 D. Tang, J. Liu, X. Wu, R. Liu, X. Han, Y. Han, H. Huang, Y. Liu and Z. Kang, *ACS Appl. Mater. Interfaces*, 2014, **6**, 7918.
24 R. Chen, G. Sun, C. Yang, L. Zhang, J. Miao, H. Tao, H. Yang, J. Chen, P. Chen and B. Liu, *Nanoscale Horiz.*, 2016, **1**, 156.

25 Z. Lu, W. Xu, W. Zhua, Q. Yang, X. Lei, J. Liu, Y. Li, X. Sun and X. Duan, *Chem. Commun.*, 2014, **50**, 6479.
26 Z. Li, M. Shao, H. An, Z. Wang, S. Xu, M. Wei, D. G. Evans and X. Duan, *Chem. Sci.*, 2015, **6**, 6624.
27 X. Long, S. Xiao, Z. Wang, X. Zheng and S. Yang, *Chem. Commun.*, 2015, **51**, 1120.
28 Z. Zhang, J. Hao, W. Yang and J. Tang, *RSC Adv.*, 2016, **6**, 9647.
29 W. Tu, J. Lei, L. Ding and H. Ju, *Chem. Commun.*, 2009, **45**, 4227.
30 S. O. Obare, T. Ito, M. H. Balfour and G. J. Meyer, *Nano Lett.*, 2003, **3**, 1151.
31 F. Song and X. Hu, *J. Am. Chem. Soc.*, 2014, **136**, 1648.
32 L. Li, R. Ma, Y. Ebina, K. Fukuda, K. Takada and T. Sasaki, *J. Am. Chem. Soc.*, 2007, **129**, 8000.
33 Z. Zhao, H. Wu, H. He, X. Xu and Y. Jin, *Adv. Funct. Mater.*, 2014, **24**, 4698.
34 B. S. Yeo and A. T. Bell, *J. Am. Chem. Soc.*, 2011, **133**, 5587.
35 A. Bergmann, E. Martinez-Moreno, D. Teschner, P. Chernev, M. Gliech, J. F. D. Araujo, T. Reier, H. Dau and P. Strasser, *Nat. Commun.*, 2015, **6**, 8625.
36 M. Gao, Y. Xu, J. Jiang, Y. Zheng and S. Yu, *J. Am. Chem. Soc.*, 2012, **134**, 2930.
37 B. S. Yeo and A. T. J. Bell, *J. Am. Chem. Soc.*, 2011, **133**, 5587.
38 N. H. Chou, P. N. Ross, A. T. Bell and T. D. Tilley, *ChemSusChem*, 2011, **4**, 1566.
39 H. Dau, C. Limberg, T. Reier, M. Risch, S. Roggan and P. Strasser, *ChemCatChem*, 2010, **2**, 724.
40 Y. Liang, Y. Li, H. Wang and H. Dai, *J. Am. Chem. Soc.*, 2013, **135**, 2013.
41 M. T. M. Koper, *J. Electroanal. Chem.*, 2011, **660**, 254.